



This is a repository copy of *Rotor speed signature analysis-based inter-turn short circuit fault detection for permanent magnet synchronous machines*.

White Rose Research Online URL for this paper:

<https://eprints.whiterose.ac.uk/214546/>

Version: Published Version

Article:

Wei, D. orcid.org/0000-0002-9070-5746, Liu, K. orcid.org/0000-0002-3998-7194, Zhu, Z. orcid.org/0000-0001-7175-3307 et al. (3 more authors) (2024) Rotor speed signature analysis-based inter-turn short circuit fault detection for permanent magnet synchronous machines. IET Electric Power Applications, 18 (10). ISSN 1751-8660

<https://doi.org/10.1049/elp2.12469>

Reuse

This article is distributed under the terms of the Creative Commons Attribution (CC BY) licence. This licence allows you to distribute, remix, tweak, and build upon the work, even commercially, as long as you credit the authors for the original work. More information and the full terms of the licence here:

<https://creativecommons.org/licenses/>

Takedown

If you consider content in White Rose Research Online to be in breach of UK law, please notify us by emailing eprints@whiterose.ac.uk including the URL of the record and the reason for the withdrawal request.



eprints@whiterose.ac.uk
<https://eprints.whiterose.ac.uk/>

ORIGINAL RESEARCH

Rotor speed signature analysis-based inter-turn short circuit fault detection for permanent magnet synchronous machines

Dong Wei¹  | Kan Liu¹  | Zi-Qiang Zhu²  | Shichao Zhou¹ | Jianbo Wang¹ | Yongdan Chen³

¹College of Mechanical and Vehicle Engineering, Hunan University, Changsha, China

²Department of Electrical and Electronics Engineering, University of Sheffield, Sheffield, UK

³National Key Lab of Vehicle Transmission, China North Vehicle Research Institute, Beijing, China

Correspondence

Kan Liu and Jianbo Wang, No. 2, Lushan Rd, Yuelu District, Changsha, Hunan 410012, China.
Email: lkan@hnu.edu.cn and wangjianbo@hnu.edu.cn

Funding information

National Key Research and Development Program of China, Grant/Award Number: 2022YFB3403205; Youth Fund of the National Natural Science Foundation of China, Grant/Award Number: 52107044

Abstract

A rotor speed signature analysis- (RSSA-)based inter-turn short circuit (ITSC) fault diagnostic method is proposed, which is robust with regard to speed- and current-loop bandwidths of permanent magnet synchronous machine (PMSM) drive systems. Conventional ITSC fault detection solutions that rely on current signals or extra devices. Thus, an initial step of investigation on the validity of RSSA is taken for residual insulation capacity monitoring of the ITSC fault at the incipient stage. The Vold–Kalman filtering order tracking method is employed for the real-time extraction of fault features. Besides, the impact of speed- and current-loop controller bandwidths on ITSC fault diagnosis is also analysed and an Adaline estimator is designed to decouple their impacts. Finally, the effectiveness of the proposed method is verified on a faulty PMSM, which exhibits satisfying results in tracking the degradation of residual insulation, even if the phase currents are significantly distorted due to low switching frequency of the inverter.

KEYWORDS

fault diagnosis, feature extraction, permanent magnet machines

1 | INTRODUCTION

Permanent magnet synchronous machines (PMSMs) occupy a large proportion of industrial and civil equipment considering the high efficiency and torque density [1, 2]. The growing demand for PMSMs accelerates the research on fault diagnosis for electric drive systems [3]. Among electrical faults in machine drives, stator inter-turn short circuit (ITSC) faults are most frequently encountered, which is usually caused by insulation breakdown [4]. Numerous research studies relevant to the ITSC fault of PMSMs, such as the finite element analysis of faulty machine, fault characteristic modelling, fault detection and fault-tolerant control [5–10], have been reported recently, among which the detection of the ITSC fault is the most widely investigated and can be categorised into three solutions.

The model-based strategy employs the analytical model which uses signals and parameters for the derivation of the fault indicator (FI). For example, fault indicators derived from

voltages and currents [1, 11], residual signals calculated from measured and estimated signals [12, 13] and state observers [14], are employed to detect the ITSC fault. The above solutions only need a few calculations thanks to its simple structure. Nevertheless, they are also responsive to the precision of machine parameters and difficult to detect the early-state fault. The data-driven-based solution has been widely used in computer vision, natural language processing etc. due to its powerful feature representation capability [15]. For ITSC fault detection, different neural networks are employed to detect the fault based on a large volume of historic operating data [16–20]. This kind of a solution mainly focuses on the classification of different machine fault types or determining the number of short-circuited turns. The residual insulation resistance and the impact of controller bandwidths are seldom taken into account. In addition, it is quite difficult to acquire enough datasets that are independent and identically distributed under different operating conditions. The signal processing-based solution usually relies on time and

This is an open access article under the terms of the [Creative Commons Attribution](https://creativecommons.org/licenses/by/4.0/) License, which permits use, distribution and reproduction in any medium, provided the original work is properly cited.

© 2024 The Author(s). *IET Electric Power Applications* published by John Wiley & Sons Ltd on behalf of The Institution of Engineering and Technology.

frequency domain analysis to acquire the fault feature from measurable signals [21]. PMSM signals acquired by additional sensors lead to extra cost; consequently, diagnosis methods using phase currents or dq -axis currents/reference voltages measured in drive control systems are employed in reality. For example, the motor current signature analysis- (MCSA-) based method is reported as quite an effective solution in the ITSC fault detection field [4].

The above methods have achieved certain success in the field of ITSC fault diagnosis. However, the ITSC fault diagnostic accuracy could be affected by low switching frequency, which is not considered but could significantly increase the amplitudes of voltage and current harmonics. This issue will be challenging in high-power traction control systems such as traction systems in railway transit and wind turbines in which the switching frequency is usually below 1 kHz to reduce switching losses [22]. Meanwhile, changing the switching frequency will lead to changes in the actual current-loop and speed-loop controller bandwidths.

In ref. [23], the second harmonic of dq -axis reference voltages is utilised to achieve more sensitive ITSC fault detection but the influence of controller bandwidth is not considered. Besides, the impact of current-loop bandwidth on ITSC fault detection is discussed in ref. [24]. A fault detection method robust to the current controller bandwidth is proposed in ref. [25], which can detect the residual insulation resistance at the early-stage fault. However, only the impact of the current-loop controller bandwidth is investigated in the above research. Both the speed-loop and current-loop controller bandwidth are considered in ref. [26], but the employed data-driven method relies on the data volume. In addition, diagnostic methods considering the influence of low switching frequency have seldom been studied. The amplitudes of fault features in harmonics depend on not only the fault degree but also on the controller bandwidths, as a larger bandwidth will reduce the amplitude of harmonics for the input signal while increasing the amplitude of harmonics for the output signal of different controllers.

In this paper, a rotor speed signature analysis- (RSSA-) based ITSC fault detection approach is introduced under low-switching frequency control and uncertain controller bandwidths. The influences of speed- and current-loop bandwidths are analysed and decoupled using a proposed Adaline estimator. Besides, for the real-time extraction of fault features, the algorithm of the Vold–Kalman filtering order tracking (VKF-OT) is employed. The effectiveness of the proposed method is finally investigated on a faulty PMSM working under low-switching frequency, which shows good robustness against the variation of controller bandwidths and the distortion of currents compared with the conventional MCSA method. The main contributions of this study are summarised as follows: (1) an FI decoupling the impact of both speed-loop and current-loop controller bandwidths is proposed based on analytic modelling and derivation. (2) The speed model under ITSC fault is built to extract the fault feature considering the impact of the low-switching frequency of the inverter. (3) Only the speed signal

is needed for diagnosis and it does not require extra sensors, massive data or adjusting of the system structures.

2 | MODELLING AND ANALYSIS OF PMSMS WITH INTER-TURN SHORT CIRCUIT FAULT

The ITSC fault denotes an insulation degradation between any two adjacent turns. The diagram of the ITSC fault in phase A is illustrated in Figure 1, which can be divided into two segments: a healthy one (depicted in black) and a faulty one (depicted in red). In the faulty section, a resistor, denoted as R_f is introduced to mimic the residual insulation, which characterises the fault level during the initial stages of the fault. The current circulating within the shorted path is denoted as i_f . Since the two-phase and three-phase ITSC faults can lead to larger variation in the phase currents [27], only the single-phase fault is considered in this paper.

2.1 | Fault feature in dq -axis currents

The voltage equation in dq -axis for the PMSM under a normal state can be expressed as follows:

$$\begin{cases} U_d = R_s i_d + \frac{d}{dt}(L_d i_d) - \omega_e L_q i_q \\ U_q = R_s i_q + \frac{d}{dt}(L_q i_q) + \omega_e L_d i_d + \omega_e \lambda_{PM} \end{cases} \quad (1)$$

where U_d , U_q , i_d , i_q , L_d , L_q , λ_{PM} , R_s and ω_e are the dq -axis voltages, currents, dq -axis inductances, permanent magnet (PM) flux linkage, phase winding resistance and electrical angular speed, respectively. For the PMSM with the ITSC fault, Equation (1) will be re-written as follows [21]:

$$\begin{cases} U'_d = R_s i_d + \frac{d}{dt}(L_d i_d) - \omega_e L_q i_q - \frac{2}{3} R_s \mu i_f \cos \theta \\ \quad - \frac{2}{3} \omega_e L_q \mu i_f \sin \theta - \frac{2}{3} L_q \mu \frac{d}{dt}(i_f) \cos \theta + \frac{2}{3} \omega_e L_d \mu i_f \sin \theta \\ U'_q = R_s i_q + \frac{d}{dt}(L_q i_q) + \omega_e L_d i_d + \omega_e \lambda_{PM} + \frac{2}{3} R_s \mu i_f \sin \theta \\ \quad - \frac{2}{3} \omega_e L_d \mu i_f \cos \theta + \frac{2}{3} L_q \mu \frac{d}{dt}(i_f) \sin \theta + \frac{2}{3} \omega_e L_q \mu i_f \cos \theta \end{cases} \quad (2)$$

where μ represents the proportion of shorted turns to the total number of turns in each phase and θ is the electrical angle. Comparing Equation (2) with (1), the ITSC fault introduces extra

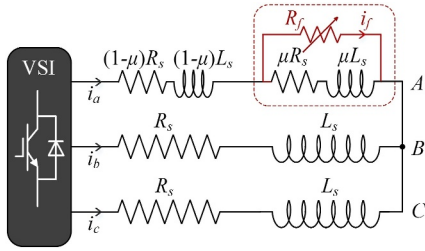


FIGURE 1 Diagram of a faulty PMSM.

components in U_d and U_q . Merging the healthy and faulty components in Equation (2) yields to the following equation:

$$\begin{cases} U_d' = R_s i_d' + \frac{d}{dt}(L_d i_d') - \omega_e L_q i_q' \\ U_q' = R_s i_q' + \frac{d}{dt}(L_q i_q') + \omega_e L_d i_d' + \omega_e \lambda_{PM} \end{cases} \quad (3)$$

i_d' and i_q' are dq -axis currents of the faulty machine, which can be expressed as follows:

$$\begin{cases} i_d' = i_d - \frac{2}{3} \mu i_f \cos \theta \\ i_q' = i_q + \frac{2}{3} \mu i_f \sin \theta \end{cases} \quad (4)$$

As shown in Figure 1, the voltage equation of the shorted circuit could be formulated as follows:

$$\begin{aligned} U_f &= i_f R_f \\ &= \mu R_s (i_a - i_f) + \mu [L M M] \frac{dI_{abc}}{dt} - \mu L \frac{di_f}{dt} + \mu \frac{d\lambda_{PM,a}}{dt} \end{aligned} \quad (5)$$

where L and M represent the self-inductance and mutual inductance in each phase, respectively. Phase currents are represented as $I_{abc} = [i_a \ i_b \ i_c]$ and $\lambda_{PM,a}$ denotes the PM flux linkage in phase A. The impact of L and M in the shorted circuit on Equation (5) is relatively insignificant [28]. The first term in Equation (5) denotes the voltage drop of the short-circuited turns whose resistance can also be ignored compared with the residual insulation resistance at the early fault stage (which cannot be ignored under a complete fault). Since the dq -axis inductances are as small as 6.5 and 2.3 mH, respectively, the second and the third items can also be ignored. Hence, the expression of i_f could be simplified as follows:

$$\begin{aligned} i_f &= \frac{\mu}{R_f} \frac{d\lambda_{PM,a}}{dt} \\ &= \frac{\mu}{R_f} \frac{d\left(\lambda_{PM,1} \cos(\theta) + \sum_{\nu=2n+1} \lambda_{PM,\nu} \cos(\nu\theta - \theta_\nu)\right)}{dt} \end{aligned} \quad (6)$$

where $\lambda_{PM,1}$ represents the magnitude of the 1st component of λ_{PM} , θ_ν indicates the phase difference between the ν -th component and the 1st component, and n denotes the natural num. Hence, i_f could be represented as follows:

$$i_f = K \frac{d\left(\cos \theta + \sum_{\nu=2\delta+1} \cos \nu(\theta - \theta_\nu)\right)}{dt} \quad (7)$$

$$= -K \omega_e \left(\sin \theta + \sum_{\nu=2\delta+1} \sin \nu(\theta - \theta_\nu) \right)$$

where $K = \frac{\mu \lambda_{PM,1}}{R_f}$ is a coefficient. Hence, ignoring the impact of high-order harmonics [28] and substituting Equation (7) to Equation (4) yields the following equation:

$$\begin{cases} i_d' = i_d + \frac{1}{3} k \omega_e \sin 2\theta \\ i_q' = i_q + \frac{1}{3} k \omega_e \cos 2\theta \end{cases} \quad (8)$$

where $k = \mu K$. As can be seen in Equation (8), the fault will mainly result in a variation of the second harmonics in i_d and i_q , which are commonly utilised for the ITSC fault diagnosis of PMSMs.

2.2 | Fault feature in rotor speed signal

Neglecting the impact of the damping coefficient, machine dynamic equilibrium equation under the faulty state will be the following:

$$T_e' - T_1 = J \frac{d\omega_m'}{dt} \quad (9)$$

where T_e' is the electromagnetic torque at the faulty state, T_1 is the shaft torque, J denotes the inertia of the rotor, ω_m indicates the mechanical angular velocity and it turns to be ω_m' under faulty state. Under steady-state operating conditions, the electromagnetic torque is assumed to be equal to the shaft torque for a healthy machine. However, the mechanical angular velocity will be affected by the ITSC fault which can be expressed as follows:

$$\omega_m' = \frac{1}{J} T_1 + \frac{1}{J} \int T_e' dt \quad (10)$$

The electromagnetic torque at the faulty state could be written as follows:

$$T_e' = \frac{3}{2} p i_q' [i_d' (L_d - L_q) + \lambda_{PM}] \quad (11)$$

where p stands for the count of pole pairs. T_e' represents a composite signal derived from i_d and i_q , potentially serving as

an alternative and efficient indicator. The electromagnetic torque in Equation (11) can be divided into two parts, reluctance torque and PM torque. The fault feature in the reluctance torque can be ignored due to the minor amplitude of inductance and the product of dq -axis currents, especially under $i_d = 0$ control. Hence, the speed will be mainly affected by the PM torque.

Combining Equations (8), (10) and (11), the mechanical angular velocity can be formulated as follows:

$$\omega_m' = -\frac{1}{J}T_1 + \frac{1}{J} \int T_e dt + \frac{kp\omega_m\lambda_{PM}}{4J} \sin 2p\theta \quad (12)$$

Which can be simplified into the following equation:

$$\omega_m' = \omega_m + \eta \sin 2p\theta \quad (13)$$

where $\eta = \frac{kp\omega_m\lambda_{PM}}{4J}$. Hence, the $2p$ th order harmonic will be the fault characteristic in speed. For the machine employed in this paper with a 24-slot 4-pole topology, the 4th-order harmonic n_{m4} will be concerned.

3 | FAULT DETECTION UNDER LOW SWITCHING FREQUENCY BASED ON RSSA

3.1 | Fault detection method based on RSSA

The increase in voltage and power levels for switching devices is accompanied by more switching losses. Reducing the switching frequency can significantly increase the output current and maintain the temperature of the IGBT at a low level. However, the number of PWM pulses in each cycle reduces, leading to less chopper voltage, more harmonics in output voltage and serious current distortion as depicted in Figure 2. The number and amplitude of harmonics have remarkably increased, especially for the lower orders which are close to the 2nd harmonic, making it difficult to extract the fault feature by MCSA methods as depicted in Figure 3a. As for the speed depicted in Figure 3b, there are many more harmonics even at the high switching frequency and the impact of the lower switching frequency is also obvious. However, the amplitude of the 4th harmonic is 10 times larger than the 2nd one of i_q . The larger amplitude of the fault characteristic harmonic in speed signal makes the fault detection results more accurate under high-level noise, especially for real-time fault detection.

The diagram illustrating the fault diagnosis method using RSSA is shown in Figure 4. The proposed method contains two parts: the controller bandwidth decoupling model part (left) and the fault detection part (right). The controller bandwidth decoupling model is trained in advance combining the deduction of the controller bandwidth model and experiment data. The adaline method is implemented to train the model based on the controller bandwidths of speed-loop and current-loop controllers, and fault feature harmonic in speed

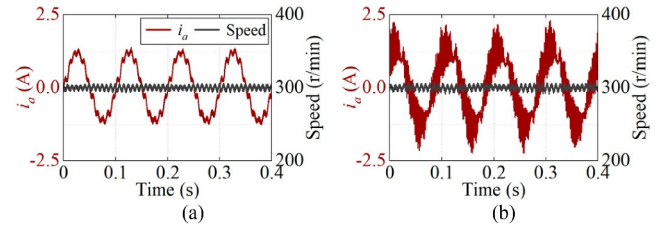


FIGURE 2 Waveforms of phase A current and speed. (a) $f_s = 10\text{ k Hz}$. (b) $f_s = 500\text{ Hz}$.

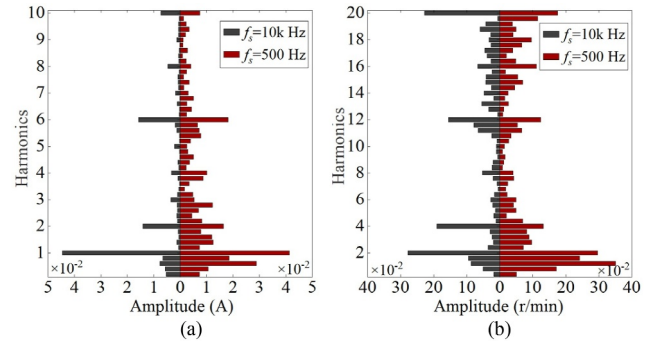


FIGURE 3 Harmonics of i_q and speed under different switching frequencies. (a) i_q . (b) Speed.

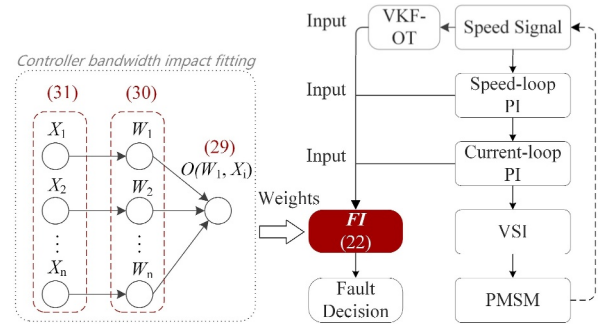


FIGURE 4 Flowchart of RSSA-based ITSC fault diagnosis considering bandwidth.

signal as inputs. The ITSC fault degree will be the output of the model. As for the fault detection part, the bandwidth information of an operating PMSM will be input into the fault detection model along with the extracted 4th harmonic from speed using VKF-OT algorithm as detailed in Appendix A. FI will be calculated in real time and a fault decision will be further provided.

3.2 | Impact of controller bandwidth on diagnosis

Ideally, speed and dq -axis current signals could be regulated to the reference constant value without any harmonics by speed-loop and current-loop controllers if the bandwidths are

sufficiently high. However, there are limits for different controller bandwidths and harmonics do exist in different signals more or less. For the speed-loop controller, the fault feature harmonic of the input signal (speed) will be suppressed as the bandwidth increase while they are raised in the output signal (i_q^*). The same pattern applies to the current-loop controller. Hence, the fault feature harmonics in speed signal will be affected by both speed-loop and current-loop controller bandwidths, which will easily lead to an incorrect assessment of the fault severity.

The proportion coefficient K_{ps} and integration coefficient K_{is} of the speed loop regulator are calculated using the following equation [29]:

$$K_{ps} = \frac{J\omega_{cs}}{1.5p\lambda_{PM}}, K_{is} = K_{ps}\omega_{cs} \quad (14)$$

where ω_{cs} is the speed controller bandwidth. According to ref. [25], the speed-loop bandwidth will have an influence on the fault feature, which can be written as follows:

$$\Delta i_q^* = (\Delta n_m^* - \Delta n_m) \left(K_{ps} + \frac{K_{is}}{s} \right) - B_a \Delta \omega_m \quad (15)$$

where Δ represents the difference between healthy and faulty states, n_m is the mechanical rotating speed and B_a is the damping coefficient.

The relation between mechanical rotating speed and the mechanical angular velocity is formulated as follows:

$$\omega_m = \frac{2\pi n_m}{60} = \frac{1}{p} \omega_e. \quad (16)$$

According to the inverse Laplace transform, Equation (14) can be written as follows:

$$\Delta i_q^* = -\frac{30\eta K_{ps}}{\pi} \sin 2p\theta - \frac{30\eta K_{is}}{\pi} \int \sin(2p\theta) d\theta - \eta B_a \sin 2p\theta \quad (17)$$

Which can be simplified as follows:

$$\Delta i_q^* = -\frac{30K_{ps} + \pi B_a}{\pi} \eta \sin 2p\theta + \frac{15\eta K_{is}}{\pi p} \cos 2p\theta. \quad (18)$$

Hence, the variation of i_q^* due to the ITSC fault under different speed-loop bandwidths can be obtained using Equation (18). Similarly, considering the feed-forward decoupling, the output of current-loop controllers can be modelled as follows:

$$\begin{cases} U_d = (i_d^* - i_d) \left(K_{pd} + \frac{K_{id}}{s} \right) + U_{d_cfs} \\ U_q = (i_q^* - i_q) \left(K_{pq} + \frac{K_{iq}}{s} \right) + U_{q_cfs} \end{cases} \quad (19)$$

where K_{pd} , K_{pq} , K_{id} and K_{iq} are the proportion and integration coefficients of the dq -axis current-loop controllers. i_d^* and i_q^* denote expected d and q -axis currents, being constant values under steady-state operating conditions. U_{d_cfs} and U_{q_cfs} are the feed-forward decoupling items.

$$K_{pd} = L_d \omega_{ci}, K_{pq} = L_q \omega_{ci}, K_{id} = K_{iq} = R_s \omega_{ci} \quad (20)$$

where ω_{ci} is the current-loop bandwidth. The impact of current loop bandwidth on the fault feature can be written as follows:

$$\begin{cases} \Delta U_d = (\Delta i_d^* - \Delta i_d) \left(K_{pd} + \frac{K_{id}}{s} \right) + \Delta U_{d_cfs} \\ \Delta U_q = (\Delta i_q^* - \Delta i_q) \left(K_{pq} + \frac{K_{iq}}{s} \right) + \Delta U_{q_cfs} \end{cases} \quad (21)$$

where Δ represents the difference between healthy and faulty states. According to the fault features Δi_d and Δi_q in Equation (8) and the inverse Laplace transform, the output of the fault feature in the current-loop controller can be derived using the following equation:

$$\begin{cases} \Delta U_d = K_{pd}(i_d' - i_d) + \int K_{id}(i_d' - i_d) d\theta - \omega_e L_q (i_q' - i_q) \\ \Delta U_q = K_{pq}(\Delta i_q^* + i_q' - i_q) + \int K_{iq}(\Delta i_q^* + i_d' - i_d) d\theta \\ + \omega_e L_d (\Delta i_q^* + i_d' - i_d) \end{cases} \quad (22)$$

Substituting Equation (8) and Equations (18–22) yield the following equation:

$$\begin{cases} \Delta U_d = \frac{1}{3} K_{pd} k \omega_e \sin 2\theta + K_{id} \int \frac{1}{3} k \omega_e \sin 2\theta d\theta \\ - \omega_e L_q \frac{1}{3} k \omega_e \cos 2\theta \\ \Delta U_q = \frac{1}{3} K_{pq} k \omega_e \cos 2\theta + K_{iq} \int \frac{1}{3} k \omega_e \cos 2\theta d\theta \\ + \omega_e L_d \frac{1}{3} K_{pd} k \omega_e \sin 2\theta + A_q \end{cases} \quad (23)$$

where

$$A_q = \frac{30K_{is} + 30K_{iq}K_{ps} + \pi B_a K_{iq}}{2\pi p} \eta \cos 2p\theta + \frac{15K_{iq}K_{is} - 60p^2 K_{ps} - 2\pi p^2 B_a}{2\pi p^2} \eta \sin 2p\theta \quad (24)$$

Considering that $\lambda_{pM,1}$ normally takes the majority proportion compared with others, hence neglecting the high order harmonics for simplicity, Equation (25) can be rewritten as follows:

$$\begin{cases} \Delta U_d = \frac{1}{3}K_{pd}k\omega_e \sin 2\theta - \frac{1}{6}k\omega_e(K_{id} + 2\omega_e L_d)\cos 2\theta \\ \Delta U_q = \frac{1}{3}K_{pq}k\omega_e \cos 2\theta + \frac{1}{6}k\omega_e(K_{iq} + 2\omega_e L_d)\sin 2\theta + A_q \end{cases} \quad (25)$$

According to Equations (18) and (25), the constant coefficients can be calculated by machine parameters. Hence, the output can be obtained by setting different bandwidth values. Ignoring high-order harmonics, the simulation results of the current- and speed-loop controller outputs are depicted in Figure 5, where the amplitudes are normalised and i_{q2} , U_{q2} and U_{d2} are the 2nd harmonic of q -axis current and dq -axis voltages. As can be seen, the current-loop bandwidth has a first-order linear impact on the output while the speed loop has a second-order linear impact on the output. However, considering the switching frequency of power devices, resistance and transient inductance of the machine, DC bus voltage and disturbance, the theoretical bandwidth value is limited and not equal to the actual value. The ignored high-order components and nonlinear saturation will also have an impact on the derived equations. Hence, the weight coefficients of bandwidths cannot be simply calculated using Equations (18) and (25).

3.3 | Bandwidth decoupling based on adaline

To reduce the impact of the bandwidth on fault degree monitoring results, a bandwidth-decoupling method is proposed

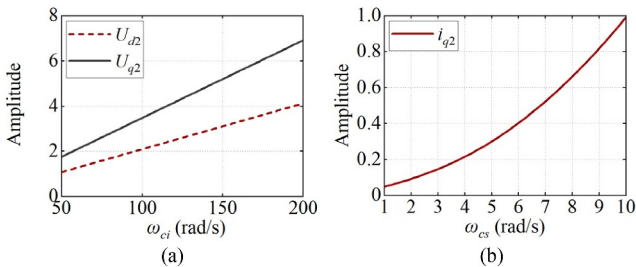


FIGURE 5 Impact of controller bandwidth. (a) U_{d2} and U_{q2} under different current controller bandwidths. (b) i_{q2} under different speed-loop controller bandwidths.

considering both the speed and current loops. The variation of the 4th harmonic in speed regarding different speed-loop bandwidths ω_{cs} and current-loop bandwidths ω_{ci} is modelled:

$$\Delta n_{m4_fit} = W_1\omega_{cs}^2\omega_{ci} + W_2\omega_{cs}^2 + W_3\omega_{cs}\omega_{ci} + W_4\omega_{cs} + W_5\omega_{ci} + D \quad (26)$$

where W_i is the weight coefficient of each item, respectively, and D is the intercept. To solve the regression equation above, the Adaline method is employed which has a less computational cost and simple architecture. The design processes of the estimator are detailed in Appendix B. After iterative training, the weights can be obtained, the FI which will be robust to speed- and current-loop bandwidths can be built as follows:

$$FI = \frac{\Delta n_{m4}}{\Delta n_{m4_fit}(\omega_{cs}, \omega_{ci})} \quad (27)$$

where Δn_{m4} is the real time extracted variation of the fourth component's magnitude of speed signal. Hence, the calculated FI by the real-time extracted n_{m4} and bandwidth values will be approximately equal to 1 for the same fault degree and different bandwidths. The amplitude of FI will increase when the ITSC fault worsens.

4 | EXPERIMENTAL VERIFICATION

4.1 | Test bench and experimental setup

The experiments are conducted on an ITSC fault test bench including two parts. One part is the specially manufactured faulty machine as shown in Figure 6a which contains an IPMSM (1) with certain coils tapped out from the stator, a 5-grade switch (2) for different shorted turns and a variable resistor (3) simulating residual insulation resistance. The other is the experimental bench consisting of the faulty machine (1), a loading motor (2), a dSPACE controller (3), a motor drive (4) and a computer (5). The parameters of the faulty machine are shown in Table 1. A schematic diagram of the test system sketching configuration of windings is shown in Figure 7. Experiments are conducted at 1000 Hz switching frequency except as otherwise noted. The control method is field-

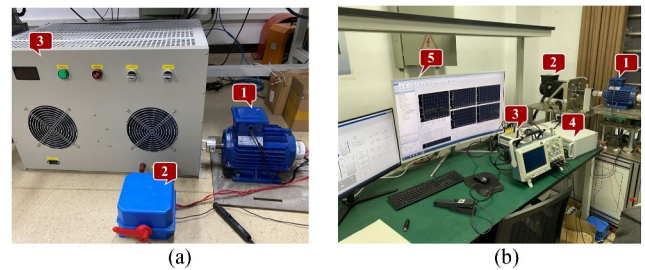


FIGURE 6 Test platform. (a) ITSC faulty machine. (b) Experimental bench.

oriented control with $i_d = 0$. The sampling frequency is set to 50 kHz, which is much greater than the minimum sampling frequency of 533 Hz calculated using the Nyquist Sampling theorem, considering 1000 r/min rated speed, 4th harmonic, 2 pole pairs and 4 times the highest frequency of the signal. The measured and finite element method (FEM) predicted line back-EMFs of the IPMSM are depicted in Figure 8. The fundamental waveform exhibits non-sinusoidal characteristics, with clear prominence of the 7th, 11th and 13th harmonics. These features are attributed to the 24-slot 4-pole and the single-chain winding design. Still, the amplitude of the fundamental component accounts for the most part and hence the other components can be ignored in Equation (8).

4.2 | Validation of proposed RSSA method

To validate the deduced fault feature in Section 2, experiments under various speed and fault conditions are performed. The correlation between the harmonics of different signals and the ITSC fault degree are analysed. The covariance matrices are

TABLE 1 Parameters of experimental IPMSM.

Parameter	Value	Parameter	Value
Rated power (kW)	2.2	d -axis inductance (mH)	23
Rated speed (r/min)	1000	q -axis inductance (mH)	65
Rated voltage (V)	380	Rated current (A)	3.8
Number of pole pairs	2	Number of turns per phase	200

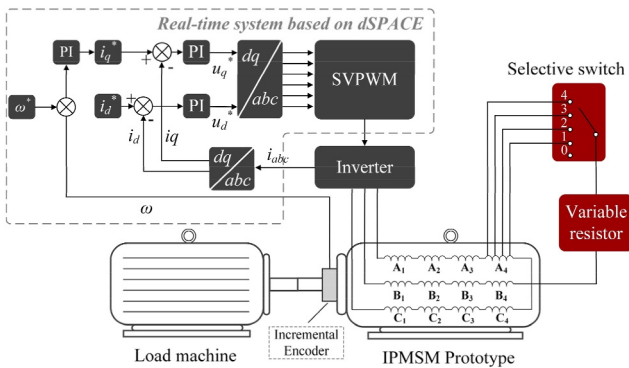


FIGURE 7 Schematic diagram of test system sketching configuration of windings.

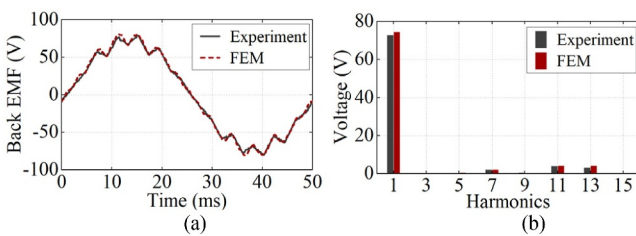


FIGURE 8 Comparison of experimentally tested and FEM simulated back-EMFs of tested IPMSM. (a) Waveforms. (b) Spectra.

introduced to represent the degree of correlation between two variables. Firstly, the amplitudes of 1~14th harmonics are extracted from phase currents, speed, dq -axis currents and dq -axis reference voltages for different shorted turns, while higher order harmonics are neglected because of their low values. The covariances between an array M representing the shorted ratio and an array A representing the amplitude of each order harmonic which corresponds to the shorted ratio are then calculated using the following equation:

$$\text{cov}(A, M) = \frac{\sum_{i=1}^n (A_i - E(A))(M_i - E(M))}{n} \quad (28)$$

where $M = [0\%, 8.5\%, 12\%, 17\%, 19.5\%]$, $E(A)$ and $E(M)$ denotes the average values of array A and M and $n = 5$. Covariance is employed because the absolute amplitude of harmonics in each signal is also a significant index for fault detection based on indicating the relevance. Each calculated $\text{cov}(A, M)$ corresponds to one coloured block in the heat map as illustrated in Figure 9 after being normalised. The y -axis represents different measurable signals and the x -axis denotes the 2~14th harmonic of each signal in the y -axis. Hence, each coloured block denotes a certain harmonic of a certain signal. The colour of each block represents the correlation between the harmonics of different signals and ITSC fault degree. Red indicates a strong correlation, which means the amplitude of a harmonic increases as the fault worsens. On the contrary, black indicates no association. Hence, it can be seen that the 4th harmonic of n_m has the strongest correlation with the ITSC fault degree under both 300 and 600 r/min. The 2nd harmonic of u_q also shows good correlation but it is easily affected by the bandwidth. The amplitudes of the second harmonics in i_d and i_q still show approximately linear relationships with the shorted turns ratio but their amplitudes are much smaller.

Figure 10 shows the amplitude variation regarding the increase of shorted turns of the 4th-order harmonic in speed n_{m4} , the second harmonics in i_{d2} , i_{q2} , U_{d2} and U_{q2} at 300 r/min. The impact of residual insulation is also investigated in Figure 11. As μ increases and R_f decreases, the amplitude of the 4th harmonic in speed rises rapidly, especially when the residual insulation deteriorates less than 5Ω . It is demonstrated that the severity of the ITSC fault depends on both μ and R_f . Furthermore, more turns will be short-circuited till the residual insulation capacity worsens to a certain degree.

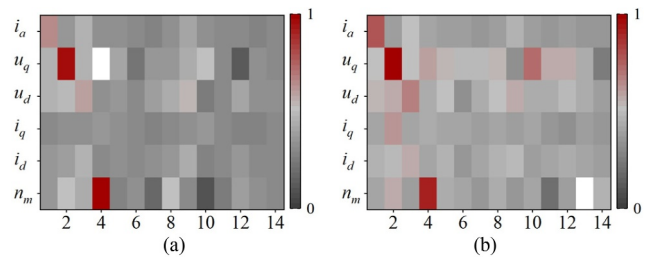


FIGURE 9 Correlation between harmonics of different signals and ITSC fault degree. (a) 300 r/min. (b) 600 r/min.

The signals before and after the fault are shown in Figure 12. On the one hand, the ITSC fault increases the amplitudes of the harmonics as depicted in most signals. On the other hand, the effective turns to produce magnetomotive force (MMF) are reduced due to the fault which also produces a reversed magnetic field causing more reduction in the MMF.

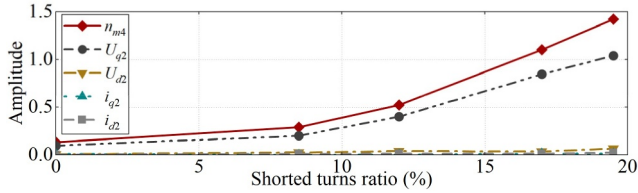


FIGURE 10 Harmonics amplitude variation of different signals along with increase of shorted turn ratio under 300 r/min speed.

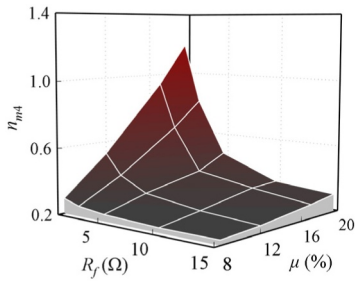


FIGURE 11 Impact of different μ and R_f on n_{m4} under 600 r/min speed.

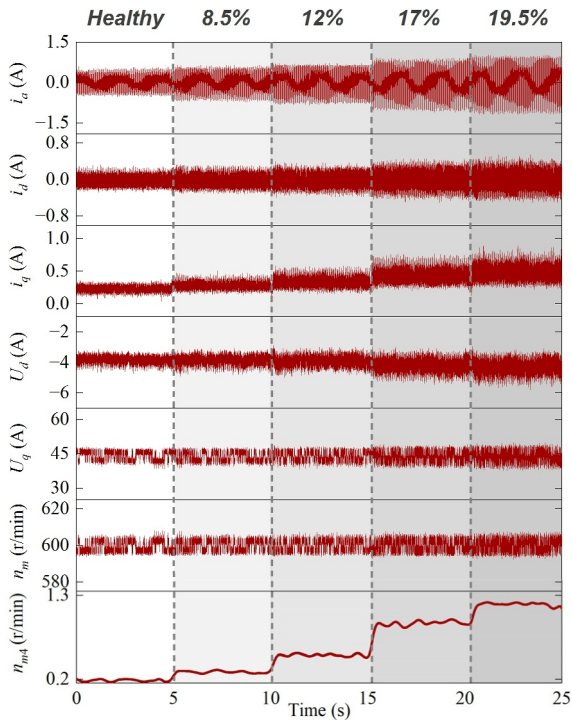


FIGURE 12 Comparison of waveforms of phase current, dq -axis currents and reference voltages, speed and FI under various fault states with 600 r/min speed.

Hence, a larger amplitude of the current is required under the same operating condition for i_a and i_q . With the increase of shorted turns, the aforementioned feature turns to be more apparent. It should be noted that the amplitude of U_q and speed signals also increase with the fault degree, but the slight changes cannot be observed compared with their amplitudes. The continuously extracted 4th harmonic of rotor speed using VKF-OT tracks the variation of shorted turns as shown in Figure 12.

4.3 | Residual insulation degradation monitoring

For the incipient ITSC fault, the residual insulation resistance between the adjacent shorted turns will gradually deteriorate until more ambient turns are shorted due to durative heat. Hence, detecting the fault and maintaining continuous fault degree variation monitoring are critical. The degradation of the insulation cannot be directly followed, but its deterioration trend could be indirectly monitored by extracting the fault feature component in the speed signal, which is related to the fault degree. The amplitude of the fault feature harmonic will increase with insulation deterioration due to the increasing fault current i_f as simulated by the FEM model in Appendix C.

Experiments imitating the residual insulation resistance are implemented by decreasing the resistance value. As depicted in Figure 13a, the magnitude of real-time extracted 4th harmonic using VKF-OT fluctuates around 0.4 and gradually increases to 1.1 which conforms to the fault degree variation. Likewise, the FI and harmonic extraction methods are valid under 600 and 900 r/min speed conditions. The proposed method is also

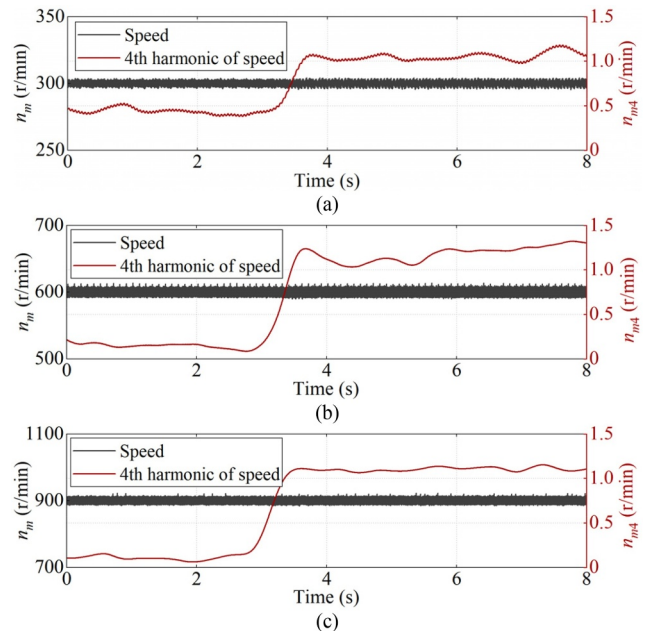


FIGURE 13 Real-time extracted 4th harmonic of speed signal while R_f decreases from 20 to 0.1 Ω with $\mu = 8.5\%$ at 1 kHz switching frequency. (a) 300 r/min. (b) 600 r/min. (c) 900 r/min.

verified at 500 and 2 kHz as depicted in Figure 14. As can be seen, the process of insulation deterioration still can be accurately monitored at different switching frequencies.

However, as the switching frequency of inverter increases, the available bandwidth of the speed loop increases, which will result in better suppression of harmonics for the input of speed-loop controller and therefore lead to a lower amplitude of fault feature harmonic. As depicted in Figures 13 and 14, after the ITSC fault occurs, the amplitudes of n_{m4} are around 1.5, 1.3 and 1 under 500, 1000 and 2000 Hz switching frequencies, respectively. Hence, the proposed method has the advantage of fault feature extraction under lower switching frequencies.

In addition, it can be seen in Figure 3 that there is much noise existing in the speed signal even around the fault feature component, especially when the inverter operates under low switching frequency. In this situation, the VKF-OT method could still effectively extract the fault feature harmonic in the speed signal of quite a small amplitude. Hence, the proposed method has good robustness with regard to noise under different operating speeds and switching frequencies.

The proposed method can also effectively extract the fault feature under varying load conditions as shown in Figure 15.

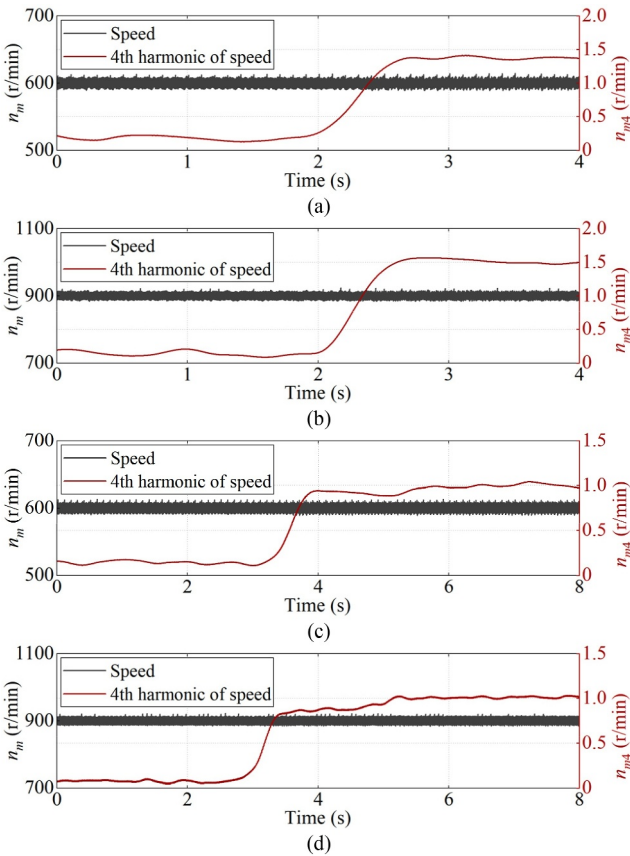


FIGURE 14 Real-time extracted 4th harmonic of speed signal while R_f decreases from 20 to 0.1 Ω with $\mu = 8.5\%$. (a) 600 r/min with 500 Hz switching frequency. (b) 900 r/min with 500 Hz switching frequency. (c) 600 r/min with 2 kHz switching frequency. (d) 900 r/min with 2000 Hz switching frequency.

The load varies from 1 Nm to 3 Nm continuously as shown in Figure 15a; however, the amplitude of the extracted harmonic increases with the load as shown in Figure 15b.

4.4 | Fault indicator with decoupling of bandwidth

The waveforms of different signals under increasing current-loop bandwidth value are shown in Figure 16. With the increase in the regulating capacity of the PI controller, the amplitude of speed and i_q are slightly reduced at the expense of amplitude raising of U_q . Figure 17 shows the tendency of the fault feature in speed concerning the speed-loop and current-loop controller bandwidths. Ten points in total are configured for the speed-loop bandwidth value with an equal interval and 12 points are set for the current loop, which are both normalised. As can be seen, the amplitude of the 4th harmonic variation in speed signal Δn_{m4} increases with the change of both ω_{cs} and ω_{ci} in an approximately linear trend in most areas.

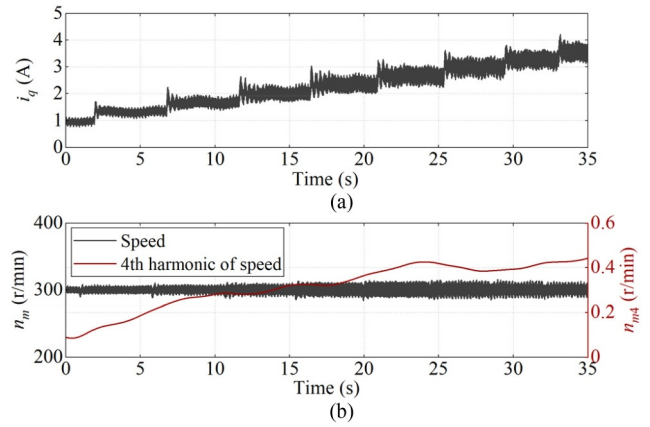


FIGURE 15 Real-time extracted 4th harmonic of speed signal under $R_f = 1 \Omega$ and $\mu = 8.5\%$ fault at 1 kHz switching frequency with 1 Nm to 3 Nm varying load. (a) i_q . (b) Speed and 4th harmonic.

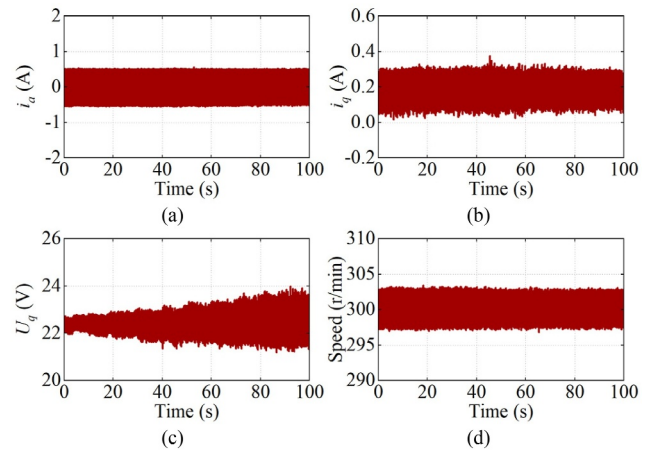


FIGURE 16 Waveforms of different signals under increasing bandwidth value in the current loop at 300 r/min. (a) i_a . (b) i_q . (c) U_q . (d) Rotor speed.

However, the amplitude stops growing and even declines when the speed-loop and current-loop bandwidths exceed certain values which represent the regulation capability and this will no longer change. Hence, only the linear area is considered.

Figure 18 shows the comparison between the directly extracted Δn_{m4} and the proposed FI using the training dataset to test the performance of the FI 's robustness against bandwidth variation. As can be seen, the FI s fluctuate around 1 regardless of the variation of ω_{cs} and ω_{ci} in the linear area. In addition, the generalisation capability of the FI is also verified using the test data under completely different speed- and current-loop bandwidths from the training dataset, which includes the data within ($\omega_{cs} = 0.35, 0.55, 0.75$) and outside ($\omega_{cs} = 0.05$) the range of the training data. As depicted in Figure 19, the FI still shows good robustness to the bandwidth change in the linear area.

4.5 | Methods comparison

To demonstrate the advantages of the RSSA-based method under low inverter switching frequency, a comparison with the traditional current signal-based method and discrete wavelet transform (DWT) method is implemented. For a fair

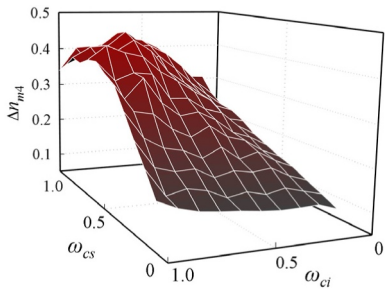


FIGURE 17 Variation of fault feature harmonic under different speed-loop and current-loop control bandwidths at 300 r/min.

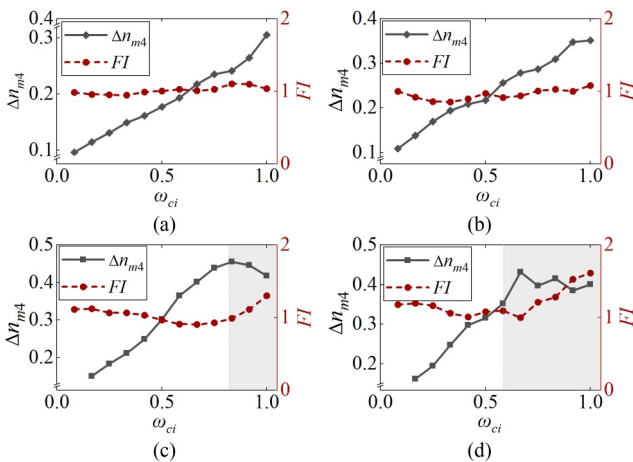


FIGURE 18 Comparison between Δn_{m4} and FI using training data under different ω_{ci} at 300 r/min. (a) $\omega_{cs} = 0.1$. (b) $\omega_{cs} = 0.3$. (c) $\omega_{cs} = 0.7$. (d) $\omega_{cs} = 0.9$.

comparison, the same experimental data are employed, which are consistent with the signals in Figure 13.

Firstly, the fault feature of the current signal is extracted by VKF-OT. The 2nd components in i_d and i_q are widely employed as FI [9, 21, 24], and the second harmonic of i_q is selected for comparison due to its larger amplitude than that in d -axis current. As shown in Figure 20a, the amplitude of the 2nd harmonic of i_q , which is i_{q2} , is too small to be effectively extracted under 300 r/min. The variation tendency of i_{q2} is not in accord with the fault deterioration condition due to the minor amplitude. In Figure 20b, the fault worsening process can be monitored at a relatively high speed, but the extracted amplitude is much smaller than the speed signal as shown in Figure 13c. Hence, the current signal has a weaker fault characteristic compared with speed under low switching frequency.

Besides, the fault feature extraction method is also compared with the DWT method, which shows effectiveness in recent research [11, 21]. The results are shown in Figure 21 based on the FI built in ref. [21], which is the proportion of the energy of the detail component where the fault feature component distributes to the overall energy of the signal. It is evident that the insulation deterioration cannot be detected under 300 r/min and the amplitude of the FI is extremely small, while the fault can be monitored under 900 r/min. However, the amplitude is still quite small due to the low proportion of the fault feature component. Hence, the

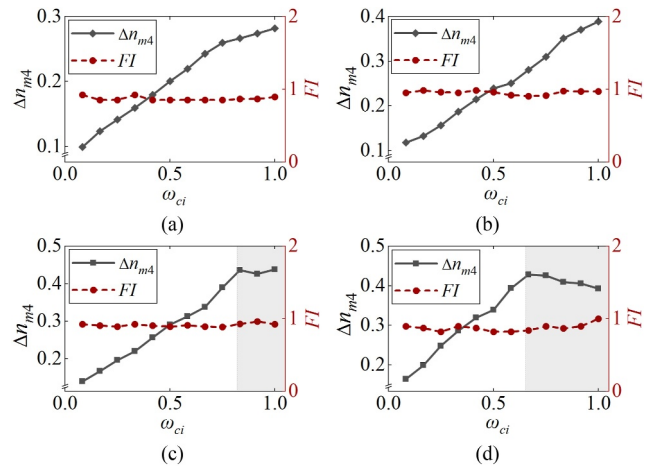


FIGURE 19 Comparison between Δn_{m4} and FI using test data under different ω_{ci} at 300 r/min. (a) $\omega_{cs} = 0.05$. (b) $\omega_{cs} = 0.35$. (c) $\omega_{cs} = 0.55$. (d) $\omega_{cs} = 0.75$.

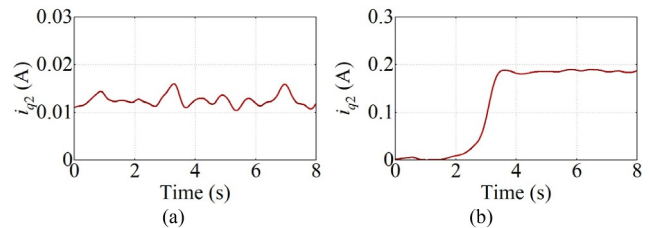


FIGURE 20 Real-time extracted 2nd harmonic of i_q while R_f decreases from 20 to 0.1 Ω with $\mu = 8.5\%$ at 1000 Hz switching frequency. (a) 300 r/min. (b) 900 r/min.

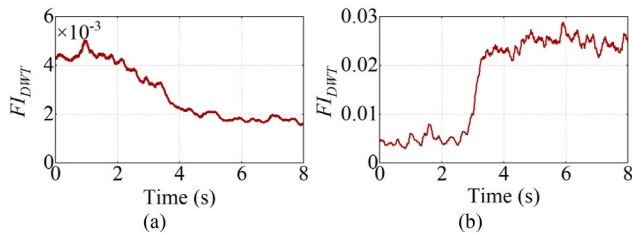


FIGURE 21 Fault indicator built based on DWT while R_f decreases from 20 to 0.1 Ω with $\mu = 8.5\%$ at 1000 Hz switching frequency. (a) 300 r/min. (b) 900 r/min.

variation is not as obvious as that in Figure 13, easily leading to misjudgements. In addition, the detail component containing the fault feature needs to be recalculated when the speed changes and the computational workload does not allow real-time operation.

5 | CONCLUSION

An RSSA-based ITSC fault diagnosis approach is proposed, which shows good accuracy under low-switching frequency control and uncertain controller bandwidths. Different from conventional ITSC fault detection methods that rely on current/voltage signals or extra devices, the proposed method uses the rotor speed for fault diagnosis; and the variation of residual insulation can be monitored at the early-stage fault. The VKF-OT algorithm is employed for the real-time extraction of fault features. An investigation is also conducted into the influence of the bandwidths of the speed- and current-loop controllers on the diagnosis of ITSC faults, and an Adaline estimator is therefore designed to decouple their influence. Compared with the conventional MCSA-based method, the experiment results show that the proposed RSSA-based method has quite good robustness against the variation of controller bandwidths and distortion of currents due to low-switching frequency. However, the proposed method does not simultaneously take the impact of speed and load variation into account, which will be further explored in future work.

AUTHOR CONTRIBUTIONS

Dong Wei: Conceptualization; data curation; formal analysis; investigation; methodology; resources; validation; writing – original draft; writing – review & editing. **Kan Liu:** Formal analysis; methodology; project administration; supervision; writing – review & editing. **Zi-Qiang Zhu:** Formal analysis; writing – review & editing. **Shichao Zhou:** Data curation; validation; writing – review & editing. **Jianbo Wang:** Investigation; writing – review & editing. **Yongdan Chen:** Investigation; writing – review & editing.

ACKNOWLEDGEMENTS

This work was supported by the National Key Research and Development Program of China under grant 2022YFB3403205

and Youth Fund of the National Natural Science Foundation of China (52107044).

CONFLICT OF INTEREST STATEMENT

The authors of this paper declare that they have no conflicts of interest regarding the research presented.

DATA AVAILABILITY STATEMENT

Data sharing is not applicable to this article as no new data were created or analysed in this study.

ORCID

Dong Wei  <https://orcid.org/0000-0002-9070-5746>

Kan Liu  <https://orcid.org/0000-0002-3998-7194>

Zi-Qiang Zhu  <https://orcid.org/0000-0001-7175-3307>

REFERENCES

- Xu, Z., Zhang, J., Cheng, M.: Investigation of signal injection methods for fault detection of PMSM drives. *IEEE Trans. Energy Convers.* 37(3), 2207–2216 (2022)
- Zhang, Z., et al.: An embedded fault-tolerant control method for single open-switch faults in standard PMSM drives. *IEEE Trans. Power Electron.* 37(7), 8476–8487 (2022). <https://doi.org/10.1109/tpel.2022.3146216>
- Huang, W., et al.: Open-circuit fault detection in PMSM drives using model predictive control and cost function error. *IEEE Trans. Transport. Electrific.* 8(2), 2667–2675 (2022). <https://doi.org/10.1109/tte.2021.3135039>
- Gandhi, A., Corrigan, T., Parsa, L.: Recent advances in modeling and online detection of stator interturn faults in electrical motors. *IEEE Trans. Ind. Electron.* 58(5), 1564–1575 (2011). <https://doi.org/10.1109/tie.2010.2089937>
- Wan, Y., et al.: Research on interturn short-circuit characteristic of the high-speed permanent-magnet machine with gramme-ring Windings. *IEEE Trans. Magn.* 58(8), 1–6 (2022). <https://doi.org/10.1109/tmag.2022.3148108>
- Ray, S., Dey, D.: Development of a comprehensive analytical model of induction motor under stator interturn faults incorporating rotor slot harmonics. *IEEE Trans. Ind. Electron.* 70(2), 2037–2047 (2023). <https://doi.org/10.1109/tie.2022.3165294>
- Chen, H., et al.: A novel online method for locating fault coil in direct-drive permanent magnet synchronous motor with inter-turn short-circuit fault using search coil array. *IET Electr. Power Appl.* 17(2), 232–244 (2023). <https://doi.org/10.1049/elp2.12258>
- Chen, B.Z., et al.: Incipient interturn short-circuit fault diagnosis of permanent magnet synchronous motors based on the data-driven digital twin model. *IEEE Trans. Emerg. Sel. Topics Power Electron.* 11(3), 3514–3524 (2023). <https://doi.org/10.1109/jestpe.2023.3255249>
- Wang, B., et al.: Stator turn fault detection by second harmonic in instantaneous power for a triple-redundant fault-tolerant PM drive. *IEEE Trans. Ind. Electron.* 65(9), 7279–7289 (2018). <https://doi.org/10.1109/tie.2018.2793188>
- Zhang, J., Zhan, W., Ehsani, M.: Diagnosis and fault-tolerant control of permanent magnet synchronous motors with interturn short-circuit fault. *IEEE Trans. Control Syst. Technol.* 31(4), 1909–1916 (2023). <https://doi.org/10.1109/tcst.2023.3239426>
- Fang, J., et al.: Improved ZSVC-based fault detection technique for incipient stage inter-turn fault in PMSM. *IET Electr. Power Appl.* 13(12), 2015–2026 (2019). <https://doi.org/10.1049/iet-epa.2019.0016>
- Hu, R., et al.: Current-residual-based stator interturn fault detection in permanent magnet machines. *IEEE Trans. Ind. Electron.* 68(1), 59–69 (2021). <https://doi.org/10.1109/tie.2020.2965500>
- Ullah, Z., Lee, S., Hur, J.: A Torque angle-based fault detection and identification technique for IPMSM. *IEEE Trans. Ind. Appl.* 56(1), 170–182 (2020). <https://doi.org/10.1109/tia.2019.2947401>

14. Hang, J., et al.: A voltage-distortion-based method for robust detection and location of interturn fault in permanent magnet synchronous machine. *IEEE Trans. Power Electron.* 37(9), 11174–11186 (2022). <https://doi.org/10.1109/tpel.2022.3167439>
15. Wang, Y., Fang, S., Hu, J.: Active disturbance rejection control based on deep reinforcement learning of PMSM for more electric aircraft. *IEEE Trans. Power Electron.* 38(1), 406–416 (2023). <https://doi.org/10.1109/tpel.2022.3206089>
16. Alipoor, G., et al.: Incipient detection of stator inter-turn short-circuit faults in a Doubly-Fed Induction Generator using deep learning. *IET Electr. Power Appl.* 17(2), 256–267 (2022). <https://doi.org/10.1049/elp2.12262>
17. Parvin, F., et al.: A comprehensive interturn fault severity diagnosis method for permanent magnet synchronous motors based on transformer neural networks. *IEEE Trans. Ind. Inf.* 19(11), 10923–10933 (2023). <https://doi.org/10.1109/tii.2023.3242773>
18. Shih, K.-J., et al.: Machine learning for inter-turn short-circuit fault diagnosis in permanent magnet synchronous motors. *IEEE Trans. Magn.* 58(8), 1–7 (2022). <https://doi.org/10.1109/tmag.2022.3169173>
19. Maraaba, L.S., et al.: Convolutional neural network-based inter-turn fault diagnosis in LSPMSMs. *IEEE Access* 8, 81960–81970 (2020). <https://doi.org/10.1109/access.2020.2991137>
20. Lee, H., et al.: Attention recurrent neural network-based severity estimation method for interturn short-circuit fault in permanent magnet synchronous machines. *IEEE Trans. Ind. Electron.* 68(4), 3445–3453 (2021). <https://doi.org/10.1109/tie.2020.2978690>
21. Hang, J., et al.: Interturn fault diagnosis for model-predictive-controlled-PMSM based on cost function and wavelet transform. *IEEE Trans. Power Electron.* 35(6), 6405–6418 (2020). <https://doi.org/10.1109/tpel.2019.2953269>
22. Gu, M., et al.: Interleaved model predictive control for three-level neutral-point-clamped dual three-phase PMSM drives with low switching frequencies. *IEEE Trans. Ind. Electron.* 36(10), 11618–11630 (2021). <https://doi.org/10.1109/tpel.2021.3068562>
23. Boileau, T., et al.: Synchronous demodulation of control voltages for stator interturn fault detection in PMSM. *IEEE Trans. Power Electron.* 28(12), 5647–5654 (2013). <https://doi.org/10.1109/tpel.2013.2254132>
24. Wei, D., et al.: Short-time adaline based fault feature extraction for interturn short circuit diagnosis of PMSM via residual insulation monitoring. *IEEE Trans. Ind. Electron.* 70(3), 3103–3114 (2023). <https://doi.org/10.1109/tie.2022.3167164>
25. Huang, S., et al.: Robust stator winding fault detection in PMSMs with respect to current controller bandwidth. *IEEE Trans. Power Electron.* 36(5), 5032–5042 (2021). <https://doi.org/10.1109/tpel.2020.3030036>
26. Wei, D., et al.: ResNet-18 based inter-turn short circuit Fault diagnosis of PMSMs with consideration of speed and current loop bandwidths. *IEEE Trans. Transport. Electrification* (2023)
27. Jäger, C., Grinbaum, I., Smajic, J.: Dynamic short-circuit analysis of synchronous machines. *IEEE Trans. Magn.* 53(6), 1–4 (2017). <https://doi.org/10.1109/tmag.2017.2661580>
28. Urresty, J., Riba, J., Romeral, L.: Diagnosis of interturn faults in PMSMs operating under nonstationary conditions by applying order tracking filtering. *IEEE Trans. Power Electron.* 28(1), 507–515 (2013). <https://doi.org/10.1109/tpel.2012.2198077>
29. Instruments, T.: InstaSPIN-FOCT™ and InstaSPIN-MOTION™ User's Guide. Texas Instruments, Dallas (2017)

How to cite this article: Wei, D., et al.: Rotor speed signature analysis based inter-turn short circuit fault detection for permanent magnet synchronous machines. *IET Electr. Power Appl.* 1–13 (2024). <https://doi.org/10.1049/elp2.12469>

APPENDIX A

In the context of speed information of the rotating machine, multiple harmonics orders can be real-time extracted by VKF-OT under nonstationary conditions without any phase deviation [28]. Suppose x_k is the tracked harmonic, then the structure equation can be expressed as follows:

$$\nabla^s x_k = \varepsilon \quad (A1)$$

where ∇ represents the difference operator. s is the specified order while ε stands for the non-homogenous term. The data equation can be expressed as follows:

$$y = Cx + \eta \quad (A2)$$

where y is the measurement, η denotes the measurement error and noise and C is the output matrix. Minimise the quadratic sum of ε and η based on least square method, hence the cost function can be derived as follows:

$$J = r^2 \varepsilon^T \varepsilon + \eta^T \eta = r^2 x^T A^T A x + (y^T - x^* C^*) (y - Cx) \quad (A3)$$

The variable r represents the weighting coefficient and the superscript $*$ denotes complex conjugate. Through the process of differentiation, the tracked component can be derived as follows:

$$x_k = \left(r^2 A^T A + I \right)^{-1} C^* y \quad (A4)$$

and I denotes the identity matrix.

APPENDIX B

Figure 4 illustrates the configuration of the Adaline method and the mathematical model of an Adaline NN is shown as follows [24]:

$$O(W_i, X_i) = \sum_{i=0}^n W_i X_i \quad (B1)$$

The variable W_i denotes the net weight and the variable X_i denotes the input. An Adaline estimator of weights can be derived as given below:

$$W_i(k+1) = W_i(k) + 2\eta X_i(d(k) - O(k)) \quad (B2)$$

where

$$W_i = [W_1, W_2, W_3, W_4, W_5, D] \quad (B3)$$

$$X_i = [\omega_{cs}^2 \omega_{ci}, \omega_{cs}^2, \omega_{cs} \omega_{ci}, \omega_{cs}, \omega_{ci}, 1] \quad (B4)$$

d is the expected output and O is the output of the network. A learning rate of 0.001 is configured and a permissible error threshold of 1.6 is established. Gradient descent is employed to accelerate the iteration process.

APPENDIX C

The FEM model of the prototype machine with ITSC fault is shown in Figure C1. The simulation results of different residual insulation resistances are shown in Figure C2, which demonstrate that the fault current i_f will increase with the deterioration of residual insulation resistance R_f .

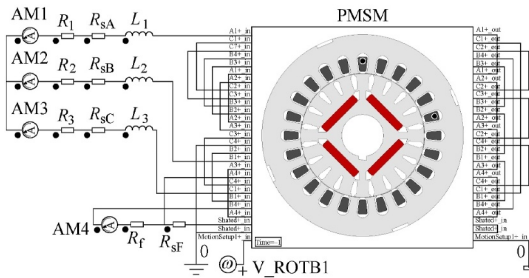


FIGURE C1 FEM model of a prototype machine with ITSC fault.

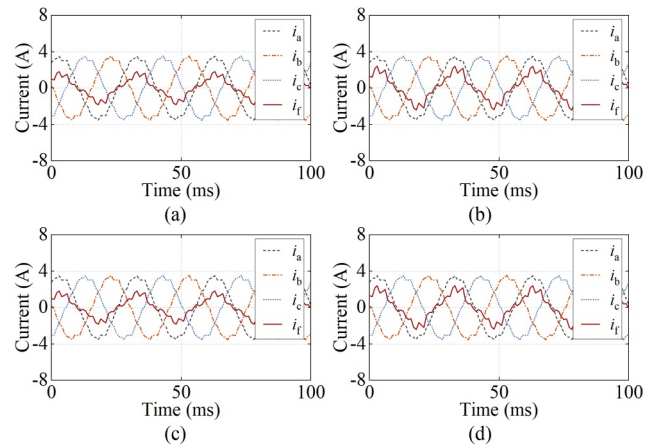


FIGURE C2 Phase current and fault current under 1000 r/min by FEM with $\mu = 8\%$ (a) $R_f = 1 \Omega$. (b) $R_f = 2 \Omega$. (c) $R_f = 3 \Omega$. (d) $R_f = 4 \Omega$.